Transition states and rearrangement mechanisms from hybrid eigenvector-following and density functional theory. Application to $C_{10}H_{10}$ and defect migration in crystalline silicon

Yuko Kumeda [a], David J. Wales [a,*], Lindsey J. Munro [b]

[a] *University Chemical Laboratories, University of Cambridge, Lensfield Road, Cambridge CB2 1EW, UK*
[b] *Department of Chemistry, University of Pittsburgh, Pittsburgh, PA 15260, USA*

Abstract

Hybrid eigenvector-following (EF) using variational eigenvector refinement and tangent space minimisation are combined with plane-wave density-functional calculations to characterise rearrangements of $C_{10}H_{10}$ and a variety of defect migration processes in crystalline silicon. For silicon we compare local and 'non-local' density functionals and supercells containing $64^{\pm 1}$ and $216^{\pm 1}$ atoms. Changes in the supercell size and the density functional can produce significant changes in the mechanisms. © 2001 Elsevier Science B.V. All rights reserved.

1. Introduction

In this Letter we couple the hybrid eigenvector-following (EF) [1,2] approach for accurate determination of transition states in large systems [3] to two popular plane-wave density-functional theory (DFT) programs. First we characterise three rearrangements of $C_{10}H_{10}$ for which previous plane-wave DFT calculations are available for comparison [4]. This relatively small system serves as a useful test to establish suitable parameters for the hybrid EF scheme and the ab initio methodology when used in combination.

We then extend our previous study [3] of defect migration in crystalline silicon, which used a tight-binding Hamiltonian, to a higher level of theory. In fact, most of the detailed mechanisms that we will report in the present work for silicon are different from those that we characterised using the tight-binding parameterised Hamiltonian. We also compare the results obtained using local and non-local density functionals and different supercells, and include results for vacancy as well as interstitial migrations.

2. Methods

2.1. DFT calculations

The CASTEP [5] and CPMD programs [6] were used to calculate all the necessary energies and gradients used by our OPTIM.2.0 program for geometry optimisation. CASTEP was employed for

---

[*] Corresponding author. Fax: +44-1223-336362.
E-mail address: dw34@cus.cam.ac.uk (D.J. Wales).

the $C_{10}H_{10}$ calculations and CPMD for silicon, in order to test the hybrid EF approach for both programs. In the CASTEP calculations we employed a cubic cell of side length 7.5 Å, ultrasoft pseudopotentials [7], a plane-wave cutoff of 490 eV (35 Ry), a Fourier transform grid of $48 \times 48 \times 48$, and an orbital convergence criterion of 5×10^{-8} eV/atom. The exchange-correlation functional used was that of Perdew et al. [8] and k-space was sampled using just the Γ-point, $k = 0$.

In the CPMD silicon calculations we compared the local density approximation (LDA) and BLYP, where the latter functional consists of Becke non-local exchange [9] and Lee–Yang–Parr correlation [10]. We also employed Kleinman–Bylander pseudopotentials [11] and an orbital convergence of 10^{-6} eV, along with a plane-wave cutoff at 163 eV (12 Ry) and the default Fourier transform grids. We have also compared results for maximum non-local pseudopotential quantum numbers, $l_{\max} = 1$ and 2, and supercells containing both $64^{\pm 1}$ and $216^{\pm 1}$ atoms, which are based upon $2 \times 2 \times 2$ and $3 \times 3 \times 3$ fragments of the crystal lattice, respectively. The ± 1 superscript is used to indicate that the vacancy calculations used cells with 63 and 215 atoms, while the interstitial calculations used cells with 65 and 217 atoms. Transition states obtained with the smaller cell were wrapped with a layer of crystalline silicon atoms before using them as starting points for geometry optimisations with the larger cell. Previous work suggests that calculations employing only the Γ-point to sample k-space are well converged for a supercell of around 216 atoms, but not for 64 [12,13], and our results agree with these conclusions. In the present work the geometry is always fully optimised, i.e., there are no frozen atoms.

2.2. Eigenvector-following

Transition states were located using the hybrid EF [1,2] approach described in our previous account [3]. We employed a variational approach to determine the smallest non-zero Hessian eigenvalue and the corresponding eigenvector; an alternative implementation of this methodology has recently been described by Henkelman and Jónsson [14]. In the variational approach we minimise a Rayleigh–Ritz ratio

$$\lambda(y) = \frac{y^t H y}{y^2} \qquad (1)$$

with respect to the vector y, where superscript t denotes the transpose. Therefore, $\lambda(y)$ becomes the smallest eigenvalue of the Hessian H and y becomes the corresponding eigenvector. The numerical second derivative of the energy is used as an approximation to $\lambda(y)$, with $E(X_0)$ the energy at point X_0 in nuclear configuration space and $\xi \ll 1$:

$$\lambda(y) \approx \frac{E(X_0 + \xi y) + E(X_0 - \xi y) - 2E(X_0)}{(\xi y)^2}. \qquad (2)$$

Differentiating (2) gives

$$\frac{\partial \lambda}{\partial y} = \frac{\nabla E(x_0 + \xi y) - \nabla E(x_0 - \xi y)}{\xi y^2} - \frac{2\lambda y}{y^2}. \qquad (3)$$

The final term in (3) was omitted from Eq. (12) in [3].

In the present hybrid EF approach we use the eigenvector obtained by minimising the above Rayleigh–Ritz ratio as the direction of uphill search, and minimise in the tangent space using a gradient-based approach. A significant speedup has been obtained by replacing the conjugate gradient minimiser used in [3] with Nocedal's limited memory BFGS (Broyden–Fletcher–Goldfarb–Shanno) routine [15]. This LBFGS algorithm was used to minimise the Rayleigh–Ritz ratio in (1) and also for the tangent space minimisation.

The present calculations allowed a maximum of 10 iterations in the variational calculation of the smallest Hessian eigenvalue and the corresponding eigenvector. There is no need to converge the eigenvector accurately at the beginning of a search (convergence only becomes important close to the transition state). Therefore, since the previous eigenvector is used as the starting point after the first step, a small number of iterations are most efficient. No tangent space minimisations were performed until the smallest non-zero eigenvector became negative and converged in two iterations or less. The variational calculation was deemed to be converged when the root-mean-square gradient specified by (3) fell below 0.15 eV Å^{-3}. If both these conditions were satisfied then up to 10

LBFGS steps were performed in the tangent space. The EF step size along the eigenvector obtained variationally was set to 0.16 Å until the corresponding eigenvalue became negative. Each stationary point optimisation was deemed to be converged when the root-mean-square gradient fell below about 0.001 eV $\mathring{A}^{-1}$. The maximum EF step size was then adjusted dynamically using a trust radius scheme with a trust ratio of 0.05 [16]. The diagonal elements of the inverse Hessian were initially set to 0.1 for all the LBFGS minimisations. To prevent contamination of the desired eigenvector by modes corresponding to overall translation (and rotation for $C_{10}H_{10}$) a projection scheme was applied to the vector y as in previous work [3].

2.3. Pathways

For each transition state the corresponding pathway was calculated by initiating searches for minima using the LBFGS algorithm [15]. These searches were started from structures in which the atoms were displaced from the transition state geometry by distances of order 0.05 Å parallel and antiparallel to the reaction vector. The resulting pathways should be a good enough approximation to the true steepest-descent paths for the present purposes.

The reaction pathways were characterised by calculating the cooperativity index

$$\tilde{N} = \frac{\left(\sum_i [\boldsymbol{Q}_i(s) - \boldsymbol{Q}_i(t)]^2\right)^2}{\sum_i [\boldsymbol{Q}_i(s) - \boldsymbol{Q}_i(t)]^4}, \tag{4}$$

where $\boldsymbol{Q}_i(s)$ is the position vector of atom i in minimum s. The closer the value of $\tilde{N}$ to 1, the more localised the rearrangement is. We also tabulate the distance between two minima in nuclear configuration space

$$D = \sqrt{\sum_i [\boldsymbol{Q}_i(s) - \boldsymbol{Q}_i(t)]^2}. \tag{5}$$

3. Results and discussion

3.1. $C_{10}H_{10}$

Jenkins and King [4] have reported plane-wave DFT calculations on the $C_{10}H_{10}$ system, and compared their results with previous ab initio and semi-empirical results. Our results for the geometrical parameters of this molecule are given in Table 1. As for the previous DFT study the C–H bond length is significantly different from experiment, and otherwise the results are in good agreement. The geometrical parameters of the $C_{10}H_{10}$ isomer hypostrophene also quite agree well with the previous study (Table 1).

Both pentaprismane and hypostrophene were reoptimised using the same DFT functional with a standard double-zeta [17,18] plus polarisation (DZP) Gaussian basis set. The CADPAC program [19] was employed for this purpose, and the default polarisation function exponents of 0.8 for carbon d and 1.0 for hydrogen p were used. The tabulated bond lengths for the plane-wave and Gaussian basis sets agree to within 0.03 Å and bond angles

Table 1
Structural parameters (Å and degrees) for D_{5h} pentaprismane and C_{2v} hypostrophene compared with previous results

Pentaprismane	1–1′	1–2	C–H	θ	ϕ	
Present work plane-waves/BLYP	1.55	1.54	1.09	119.6	123.1	
Present work DZP basis/BLYP	1.56	1.55	1.08	119.4	123.3	
Previous DFT [4]	1.58	1.57	1.10	121.3	117.9	
Experiment [36]	1.57	1.55	1.00	119.2	124.2	
Hypostrophene	1–1′	2–2′	3–3′	1–2	2–3	3–4
Present work plane-waves/BLYP	1.53	1.61	2.95	1.54	1.48	1.33
Present work DZP basis/BLYP	1.54	1.60	2.96	1.55	1.51	1.33
Previous DFT [4]	1.55	1.63	2.88	1.57	1.50	1.34

The labelling scheme for bond lengths and angles is the same as [4].

agree to within 0.2°. Hypostrophene lies about 1.36 eV lower in energy than pentaprismane in the present plane-wave calculations, compared to 1.42 eV for the DZP basis and 0.2 eV in the previous plane-wave study [4]. A previous semi-empirical calculation by Gimarc and Zhao [20] also favoured a smaller difference of 0.26 eV. More definitive calculations are probably needed to resolve this energetic discrepancy. The energies of the hypostrophene molecule in different orientations varied by around 6×10^{-4} eV, providing a lower bound to the numerical error in the energy. In view of the good agreement between the Gaussian and plane-wave basis sets we did not study the effects of extended sampling of k-space for $C_{10}H_{10}$, since the main purpose of these calculations was to find suitable parameters for the hybrid EF scheme when used in conjunction with a plane-wave DFT potential.

The first transition state that we located while searching for suitable EF parameters corresponds to a relative rotation of the benzene–cyclobutadiene van der Waals complex. We omit these results since DFT with currently available functionals is not expected to describe such states properly [21]. However, it is noteworthy that the hybrid EF approach was able to provide an accurate description of stationary points and pathways in this flat region of the potential energy surface.

The second transition state located has C_{2v} symmetry and mediates a symmetric degenerate rearrangement [22] of hypostrophene, i.e., it links permutational isomers of the latter molecule (Fig. 1). The barrier is 0.87 eV, or about 7000 cm^{-1}, which might be sufficiently small for the molecule to exhibit fluxional behaviour under experimental conditions at high temperature. In each figure we show the two minima and the transition state that connects them, with the reaction vector superimposed.

The third transition state located has C_1 symmetry and mediates a non-degenerate rearrangement between pentaprismane and a tricyclic ring minimum (Fig. 1). The barriers are 2.2 and 3.2 eV, respectively, indicating that the tricyclic ring lies about 1.0 eV lower in energy than pentaprismane, at this level of theory.

3.2. Defect migration in crystalline silicon

In the present study we have also calculated rearrangement mechanisms for interstitial and vacancy defects in crystalline silicon, using supercells of $64^{\pm 1}$ and $216^{\pm 1}$ atoms. Initial starting points for transition state searches were obtained from our previous results using a tight-binding Hamiltonian [3], with the coordinates rescaled according to the slightly different supercell sizes. For the $64^{\pm 1}$ cells the optimal cell size for the corresponding perfect diamond lattice was found to be 10.89 Å for the LDA functional with $l_{max} = 1$, and this value was also employed in the BLYP calculations. For all the $216^{\pm 1}$ supercells the cell size was set to the optimal value for the corresponding perfect crystal, which was found to be 16.69 or 16.40 Å for the BLYP functional with $l_{max} = 1$ and 2, respectively. Since our results indicate that the mechanisms calculated with the smaller cells are not converged, we did not reoptimise the BLYP stationary points with the corresponding BLYP optimal diamond cell size, or consider $l_{max} = 2$. Transition states located for $64^{\pm 1}$ supercells were used as starting points for $216^{\pm 1}$ supercell calculations by wrapping them with a layer of 152 atoms from a larger diamond lattice.

The calculation of defect formation energies for these bulk structures employs the diamond structure for 64 or 216 particles as a reference. We rescale the energy of the defect structure so that both systems contain 64 or 216 atoms. Let N' be the number of particles in the defect structure and $E_{N'}$ the corresponding energy. Then the formation energy (E_f) for the larger supercell was estimated as

$$E_f \approx \frac{216}{N'} E_{N'} - E_{216}. \tag{6}$$

We first benchmarked our calculations by calculating the vacancy formation energy for comparison with the results of Puska et al. [12]. For this calculation alone we used a fixed supercell size of 16.17 Å and a plane-wave cutoff of 204 eV (15 Ry), along with the LDA functional. We obtained vacancy formation energies of 2.49 and 3.32 eV for $l_{max} = 1$ and 2, respectively, and the latter value is
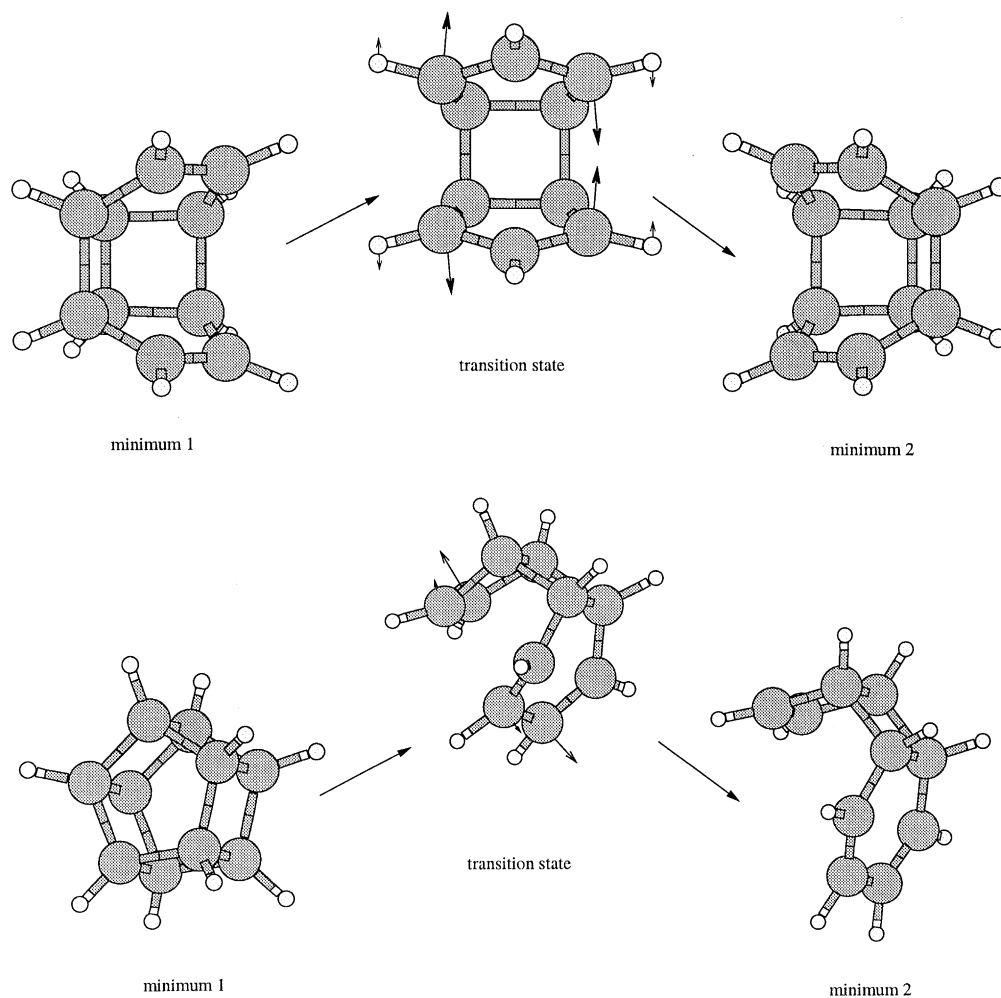
Fig. 1. Top: degenerate rearrangement of hypostrophene. Bottom: rearrangement between pentaprismane and a tricyclic ring minimum.

in good agreement with the results of Puska et al. All the numerical results reported below for silicon are for calculations with $l_{max} = 2$, since d-type functions may be important for silicon atoms in non-tetrahedral environments. We initially optimised the geometries with $l_{max} = 1$ and found that five out of seven pathways were qualitatively unaffected when we reconverged them with $l_{max} = 2$; the geometries were only slightly perturbed and the energy differences typically changed by less than 8%. However, two of the paths differed more significantly, and in both cases a hexagonal interstitial was obtained with $l_{max} = 2$ instead of a split interstitial. This result suggests that the hexagonal interstitial, containing a six-coordinate atom, is particularly stabilised by the inclusion of d functions.

For the $64^{\pm 1}$-atom cell calculations (all with $l_{max} = 1$) we found that the initial starting geometries obtained from our previous tight-binding study generally changed significantly. We also found that transition states converged with the LDA functional often changed when they were reoptimised using BLYP. Three of the pathways

calculated using the LDA and BLYP functionals are essentially the same, but the others involve at least one minimum that is structurally distinct, even when the transition states appear to be virtually identical.

In view of the lack of convergence shown by the above results we will only discuss in detail our calculations for $216^{\pm 1}$ cells with the BLYP functional and $l_{max} = 2$. In total, we located six different pathways for interstitial migration and one for vacancy migration. One of the transition states clearly corresponds to that found with the smaller cell. However, other transition states, which appear to be structurally the same as for the smaller cell, can link structurally distinct minima in the larger cell.

Characterisation of the reaction pathways for the above transition states produced seven minima corresponding to interstitial atoms, and one corresponding to the simple vacancy. The formation energies of these defects are given in Table 2, along with the results obtained using a tight-binding Hamiltonian for a 217-atom cell [3] when the structures appear to be the same. Only three of the minima correspond to those found in the previous study, and their formation energies appear to be systematically overestimated (by 15–20%) with the tight-binding potential. The $\langle 1 1 0 \rangle$-split interstitial is consistently the lowest-energy interstitial defect at each level of theory, although the formation energy of the hexagonal interstitial is the same within the accuracy of these calculations.

The results for the defect migration pathways and the corresponding transition states are collected in Table 3. Four of these pathways involve the $\langle 1 1 0 \rangle$-split interstitial, including a symmetric degenerate rearrangement [22] that corresponds to rotation of the defect (Fig. 2) [37]. The latter mechanism is localised and concerted: an atom initially on a diamond lattice site becomes part of the new interstitial, while one of the original interstitial atoms moves to a lattice site. The new interstitial lies in the $\langle \bar{1} \bar{1} 0 \rangle$ direction if the initial

Table 2
Minima and their formation energies, E_f, (in eV) for the $216^{\pm 1}$ supercell using the BLYP functional and $l_{max} = 2$

Minimum	Figure	E_f (BLYP)	E_f (TB)
$\langle 1 1 0 \rangle$	2,3	4.406	5.546
$\langle 1 0 3 3 \rangle$	3	5.122	6.106
$\langle 0 1 0 \rangle$	3	5.155	–
Hexagonal interstitial	2,4	4.456	–
min-A	4	5.106	–
min-B	4	10.951	–
min-C	4	10.805	–
Vacancy	5	3.336	3.902

Formation energies are also given for a tight-binding Hamiltonian for the three minima that are structurally equivalent. Split interstitials are labelled according to their orientation.

Table 3
Characteristics of the pathways and transition states found in the present study for the BLYP functional and $216^{\pm 1}$-atom supercells

Pathway	Figure	E_f	ΔE_1	ΔE_2	$\tilde{N}$	D	Description
$\langle 1 1 0 \rangle \rightarrow$ hexagon	2	4.629	0.222	0.172	2.33	1.79	Translation
$\langle 1 1 0 \rangle \rightarrow \langle 1 1 0 \rangle$	2	5.152	0.749	0.749	2.93	2.85	Rotation
$\langle 0 1 0 \rangle \rightarrow \langle 1 1 0 \rangle$	3	5.516	0.362	1.110	4.10	1.80	Rotation
$\langle 1 1 0 \rangle \rightarrow \langle 1 0 3 3 \rangle$	3	15.682	1.279	0.562	4.79	1.93	Rotation/Translation
min-A $\rightarrow$ hexagon	4	5.512	0.407	1.059	4.52	2.77	Rotation
min-B $\rightarrow$ min-C	4	12.663	1.719	1.867	3.69	2.33	Rotation
Vacancy $\rightarrow$ vacancy	5	3.926	0.586	0.586	2.18	2.38	Migration

Each pathway is described in terms of the minima that it links, the formation energy of the transition state, E_f, (in eV), the barrier heights ΔE_1 and ΔE_2 (in eV), the cooperativity index, $\tilde{N}$, and the distance between the minima in nuclear configuration space, D (in Å).
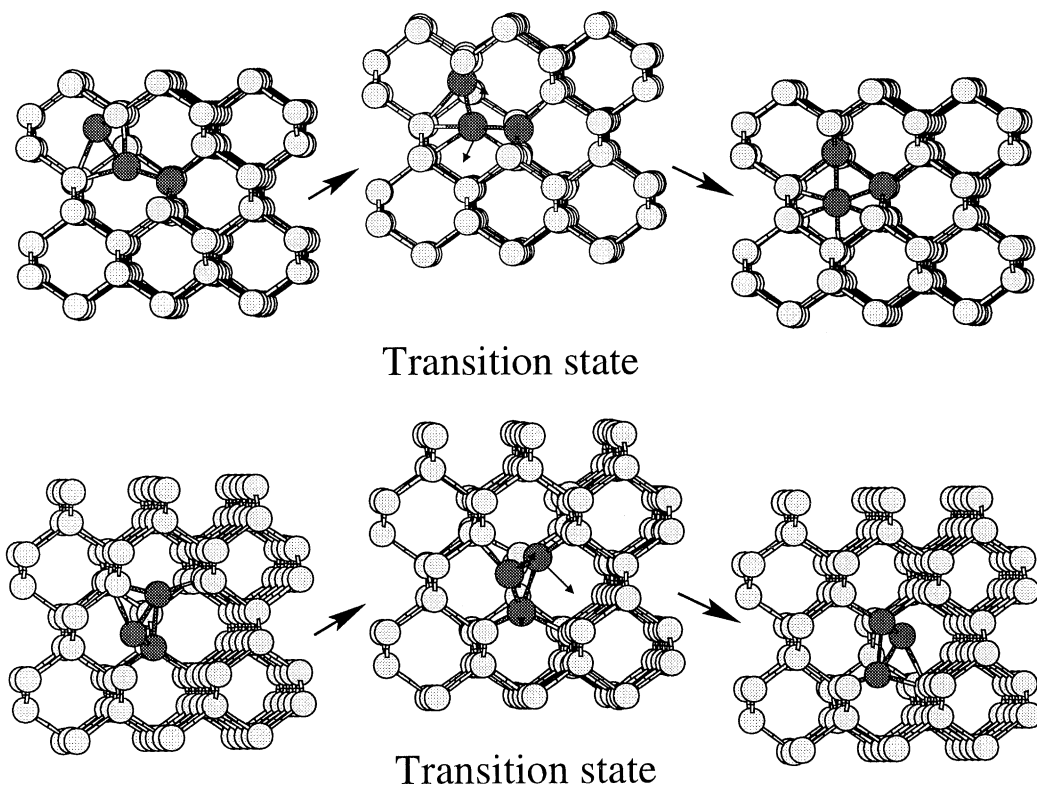
Fig. 2. $\langle 110 \rangle \rightarrow$ hexagonal interstitial (top) and $\langle 110 \rangle \rightarrow \langle 110 \rangle$ rotational (bottom) rearrangements calculated for a supercell containing 217 Si atoms using the BLYP functional. Each mechanism is mainly localised on the dark shaded atoms, and the transition vector is superimposed on both transition states.

direction is $\langle 110 \rangle$; these structures are equivalent, of course.

In fact, an alternative migration route with lower barriers is available to the $\langle 110 \rangle$-split interstitial via a hexagonal interstitial minimum (Table 3). These two rearrangements of the $\langle 110 \rangle$-split interstitial have the smallest values of the cooperativity index $\tilde{N}$, indicating that they are the most localised mechanisms. For comparison, previous theoretical and experimental values for the $\langle 110 \rangle$-split interstitial formation energy, E_f, range between 0.9 and 4.7 eV [3,13,23–31], and values for the rearrangement barrier, ΔE, range between 0.65 and 1.8 eV [24,26,31].

The $\langle 10\,3\,3 \rangle$-split interstitial found in the previous tight-binding study [3] was also located in the present work. The formation energy decreases from 6.106 eV with the tight-binding Hamiltonian to 5.122 eV for the $216^{\pm 1}$ supercell calculation

using BLYP. A pathway linking this minimum to the $\langle 110 \rangle$-split interstitial is shown in Fig. 3. The mechanism in this case is unsymmetrical, and the barriers are significantly higher than for the first two rearrangements of the $\langle 110 \rangle$-split interstitial discussed above.

We located one further pathway that links the $\langle 110 \rangle$-split interstitial to another interstitial defect, in this case the $\langle 010 \rangle$-split interstitial (Fig. 3). Four atoms are involved in this mechanism, which is again relatively localised. The barriers are intermediate between those for the degenerate rearrangement of the $\langle 110 \rangle$ interstitial and those for the $\langle 110 \rangle \rightarrow \langle 10\,3\,3 \rangle$ process.

The other minima described in Table 2 are also based upon interstitials, but they cannot be described as simply as those above. We refer to them as min-A, -B, -C. A pathway linking min-A and the hexagonal interstitial is shown in Fig. 4; the
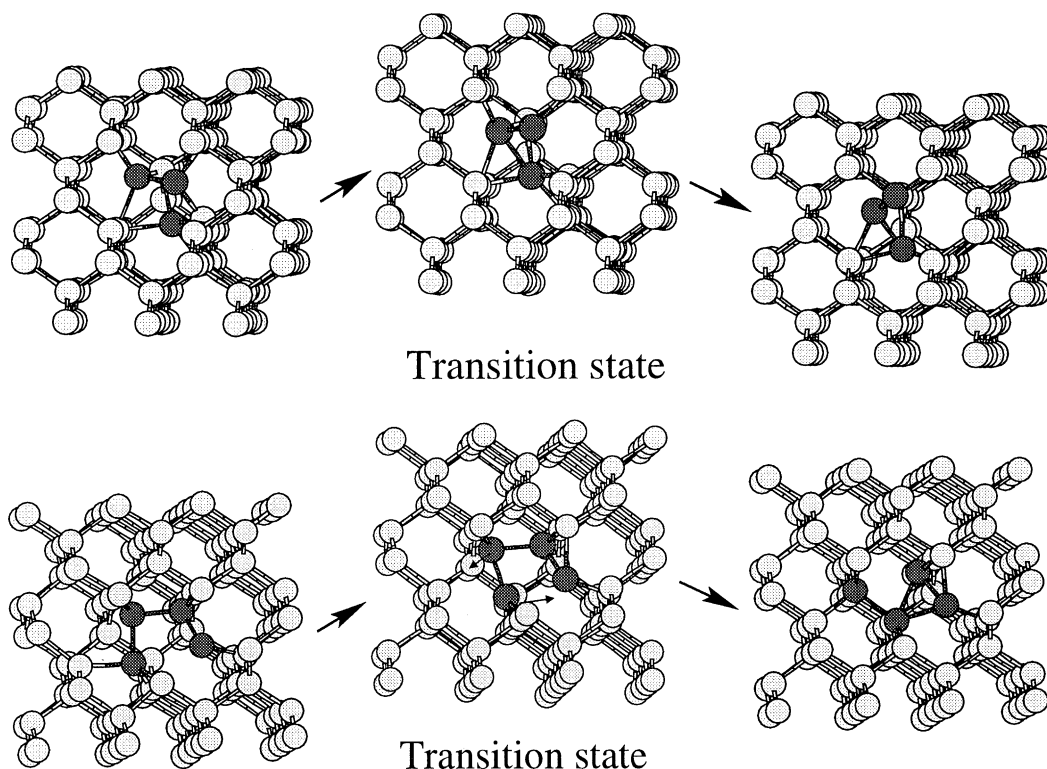
Fig. 3. $\langle 110 \rangle \rightarrow \langle 1033 \rangle$ (top) and $\langle 010 \rangle \rightarrow \langle 110 \rangle$ (bottom) rearrangements calculated for a supercell containing 217 Si atoms using the BLYP functional.

mechanism involves concerted motion of four atoms.

We also found a rearrangement corresponding to the hypothetical process suggested by Wooten, Winer and Weaire (WWW) [32] for relaxing amorphous silicon. This transition state was located during test runs where the optimisation parameters were explored, and the corresponding minima are significantly higher in energy because the supercell contains several defects. Hence, the formation energies of the corresponding stationary points are significantly higher than for the other, less defective, structures. In this process a $\langle 100 \rangle$-split interstitial is formed by an essentially localised rotation of two atoms (Fig. 4). The barrier heights of 1.719 and 1.867 eV are the largest that we have found in this study for Si. We subsequently removed the other defects that appear to be uninvolved in the rearrangement, and searched again for a transition state. Another

WWW process was found, but a 'spectator' defect formed spontaneously during the transition state search, and appears to participate in the rearrangement. We speculate that WWW processes may be more favourable in amorphous silicon.

Finally, the pathway corresponding to simple vacancy migration between nearest-neighbour lattice sites is shown in Fig. 5. This symmetric degenerate rearrangement [22] has a barrier intermediate between those for the translational and rotational symmetric degenerate rearrangements of the $\langle 110 \rangle$-split interstitial and the lowest overall activation energy, defined as the sum of the defect formation energy and the barrier. For comparison, previous theoretical and experimental values for the vacancy formation energy, E_f, range between 2.0 and 4.9 eV [3,24–27,29,33,34], and values for the rearrangement barrier, ΔE, range between 0.1 and 1.8 eV [3,24,26,29,33,35].
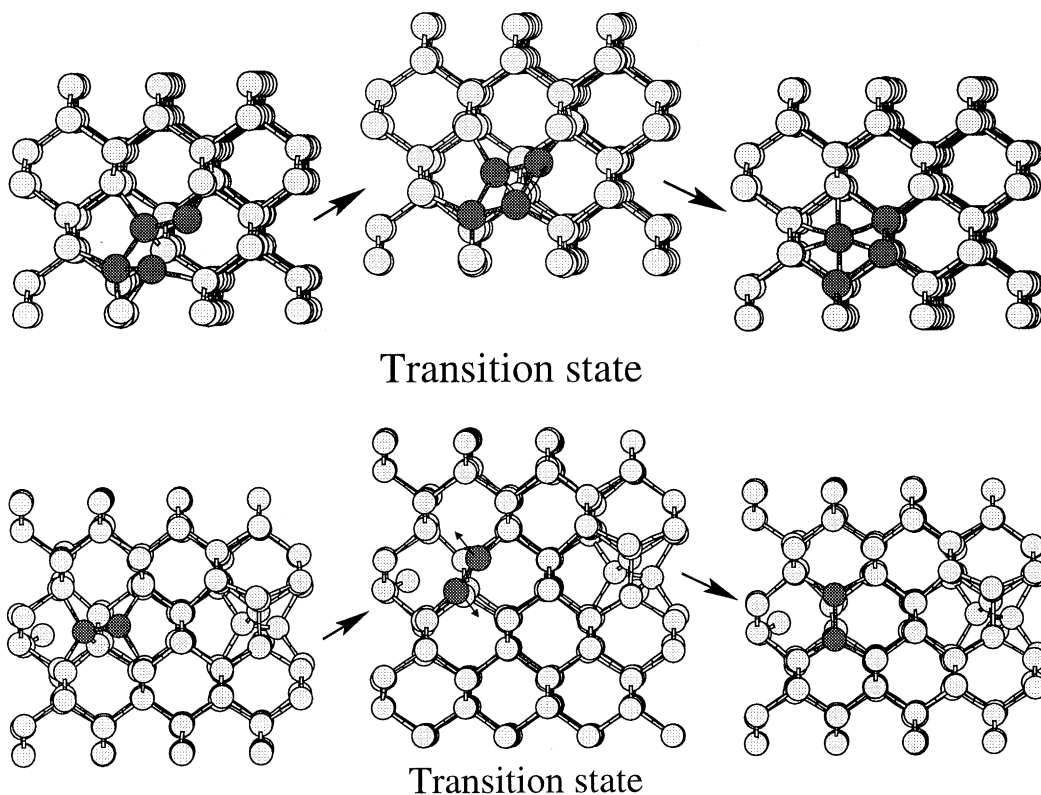
Fig. 4. min-A → hexagonal (top) and min-B → min-C (bottom) rearrangements calculated for a supercell containing 217 Si atoms using the BLYP functional.

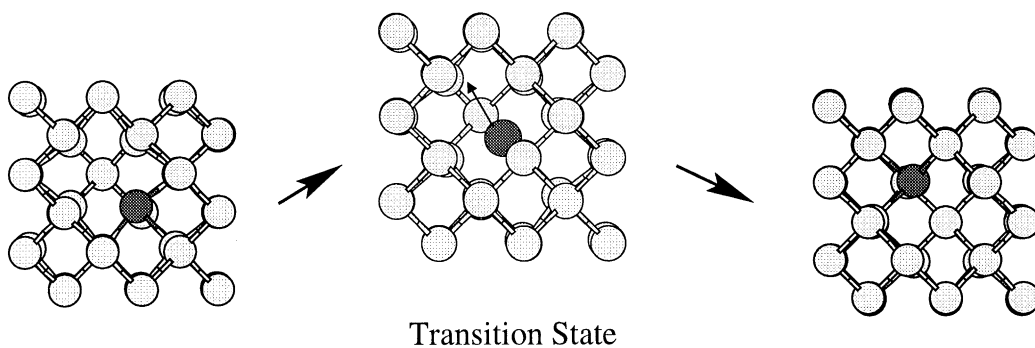

Fig. 5. Vacancy → vacancy migration pathway calculated for a supercell containing 215 Si atoms using the BLYP functional.

4. Conclusions

Transition states can be located systematically for both isolated molecules and bulk systems by hybrid-EF techniques within the plane-wave DFT framework.

For silicon, the present results show that DFT for both the LDA and BLYP exchange-correlation functionals can give different results from the tight-binding Hamiltonian used in our previous study [3]. Some of the stationary points located in the latter work are preserved in the DFT framework, in

particular the lowest-energy interstitial minimum $\langle 1\,1\,0 \rangle$-split interstitial and the vacancy minimum, but the majority are not. In fact, stationary points and pathways can also be different for the LDA and BLYP functionals, and a number of structures do not appear to be converged for a supercell size of $64^{\pm 1}$ when only the Γ point is sampled, in agreement with previous work [12,13].

The $\langle 1\,1\,0 \rangle$-split interstitial defect is found to be the lowest-energy interstitial structure, in agreement with previous calculations [3,13,23,24], but its formation energy is significantly greater than that of a simple vacancy. The latter quantity is in good agreement with previous work when consistent DFT parameters are employed. The vacancy migration pathway has the lowest total activation energy, and this process should be the main contributor to self-diffusion at low temperatures. The next lowest-energy paths correspond to diffusion of the $\langle 1\,1\,0 \rangle$-split interstitial, either via rotation or a hexagonal interstitial minimum, and these mechanisms are likely to be important at higher temperature.

We have also found pathways with significantly higher barriers corresponding to the WWW process, where a $\langle 1\,0\,0 \rangle$-split interstitial is created (or destroyed) by a local rotation of two atoms.

Acknowledgements

References

[1] C.J. Cerjan, W.H. Miller, J. Chem. Phys. 75 (1981) 2800.
[2] J. Pancíř, Coll. Czech. Chem. Commun. 40 (1975) 1112.
[3] L.J. Munro, D.J. Wales, Phys. Rev. B 59 (1999) 3969.
[4] S.J. Jenkins, D.A. King, Chem. Phys. Lett. 317 (2000) 381.
[5] M.C. Payne, M.P. Teter, D.C. Allan, T.A. Arias, J.D. Joannopoulos, Rev. Mod. Phys. 64 (1992) 1045.
[6] J. Hutter, A. Alavi, T. Deutsch, W. Silvestri, CPMD version 3.4.0, Stuttgart, 2000.
[7] N. Trouiller, J.L. Martins, Phys. Rev. B 43 (1991) 1993,8861.
[8] J.P. Perdew, J.A. Chevary, S.H. Vosko, K.A. Jackson, M.R. Pederson, D.J. Singh, C. Fiolhais, Phys. Rev. B 46 (1992) 6671.
[9] A.D. Becke, Phys. Rev. A 38 (1988) 3098.
[10] C. Lee, W. Yang, R.G. Parr, Phys. Rev. B 37 (1988) 785.
[11] L. Kleinman, D.M. Bylander, Phys. Rev. Lett. 48 (1982) 1425.
[12] M.J. Puska, S. Poykko, M. Pesola, R.M. Nieminen, Phys. Rev. B 58 (1998) 1318.
[13] S.J. Clark, G.J. Ackland, Phys. Rev. B 56 (1997) 47.
[14] G. Henkelman, H. Jónsson, J. Chem. Phys. 111 (1999) 7010.
[15] D. Liu, J. Nocedal, Math. Programming B 45 (1989) 503.
[16] D.J. Wales, J.P.K. Doye, M.A. Miller, P.N. Mortenson, T.R. Walsh, Adv. Chem. Phys. 115 (2000) 1.
[17] T.H. Dunning, J. Chem. Phys. 53 (1970) 2823.
[18] S.J. Huzinaga, J. Chem. Phys. 42 (1965) 1293.
[19] R.D. Amos, I.L. Alberts, J.S. Andrews, S.M. Colwell, N.C. Handy, D. Jayatilaka, P.J. Knowles, R. Kobayashi, K.E. Laidig, G. Laming, A.M. Lee, P.E. Maslen, et al., The Cambridge Analytic Derivatives Package Issue 6, Cambridge, 1995.
[20] B.M. Gimarc, M. Zhao, J. Org. Chem. 60 (1995) 1971.
[21] E.J. Meijer, M. Sprik, J. Chem. Phys. 105 (1996) 8684.
[22] J.G. Nourse, J. Am. Chem. Soc. 102 (1980) 4883.
[23] D.J. Chadi, Phys. Rev. B 46 (1992) 9400.
[24] M. Tang, L. Colombo, J. Zhu, T.D. De La Rubia, Phys. Rev. B 55 (1997) 14279.
[25] A. Ural, P.B. Griffin, J.D. Plummer, Phys. Rev. Lett. 83 (1999) 3454.
[26] H. Bracht, N.A. Stolwijk, H. Mehrer, Phys. Rev. B 52 (1995) 16542.
[27] P.E. Blöchl, E. Smargiassi, R. Car, D.B. Laks, W. Andreoni, S.T. Pantelides, Phys. Rev. Lett. 70 (1993) 2435.
[28] D. Maroundas, R.A. Brown, Appl. Phys. Lett. 62 (1993) 172.
[29] D. Maroundas, R.A. Brown, Phys. Rev. B 47 (1993) 15562.
[30] J. Zhu, T. Diaz de la Rubia, L.H. Yang, C. Mailhiot, G.H. Gilmer, Phys. Rev. B 54 (1996) 4741.
[31] M. Nastar, V.V. Bulatov, S. Yip, Phys. Rev. B 53 (1996) 13521.
[32] F. Wooten, K. Winer, D. Weaire, Phys. Rev. Lett. 54 (1985) 1392.
[33] M.I. Baskes, J.S. Nelson, A.F. Wright, Phys. Rev. B 40 (1989) 6085.
[34] T.J. Lenosky, J.D. Kress, I. Kwon, A.F. Voter, B. Edwards, D.F. Richards, S. Yang, J.B. Adams, Phys. Rev. B 55 (1997) 1528.
[35] N. Bernstein, E. Kaxiras, J. Phys. Rev. B 56 (1997) 10488.
[36] P. Engel, P.E. Eaton, B.K.R. Shankar, Z. Kristallogr. 159 (1982) 239.
[37] The complete pathways may be downloaded from http://brian.ch.cam.ac.uk/yuko/Sipaths.tar.gz.